

The seismic signature of upper-mantle plumes: application to the northern East-African Rift

Chiara Chiviero¹, John J. Armitage², Saskia Goes³, and James O. S. Hammond⁴

¹Dublin Institute for Advanced Studies (DIAS), Dublin D02 Y006, Ireland

²Dynamique des Fluides Géologiques, Institut de Physique du Globe de Paris, Paris, France

³Department of Earth Science and Engineering, Imperial College London, London, UK

⁴Department of Earth and Planetary Sciences, Birkbeck, University of London, London, UK

Abstract

Several recent seismic and numerical studies proposed that below some hotspots secondary smaller-scale upper-mantle plumelets rise from a regional thermal boundary layer below 660 km depth, fed by a deeper plume source. We recently found tomographic evidence of several small upper-mantle upwellings, spaced by several 100 km, rising through the transition zone below the northern East-African Rift. To better test this interpretation, we run 3D numerical simulations of mantle convection for Newtonian and non-Newtonian rheologies within a Cartesian box, for both thermal instabilities rising from the lower boundary, and the destabilisation of a thermal anomaly initially placed at the base of the box. The thermal structures are converted to seismic velocities using a mineral-physics approach. Synthetic resolution tests are then conducted for the same P- and S- data distribution and inversion parameters as our original teleseismic travel-time tomography. The models predict simultaneous plumelets in different stages of their evolution rising from a hot boundary layer located in the topmost lower mantle, resulting in seismic structure that looks substantially more complex than the simple vertical cylinders that are often anticipated. From the selection of models we find that the destabilisation of a 100 °C, 100 km thick thermal anomaly with a non-Newtonian rheology, most closely matches the spatial and temporal distribution of seismic anomalies below the rift system. However, the destabilisation of a 200 °C anomaly best matches the magnitudes of the anomalies. Finally, we find that for reasonable upper-mantle viscosities, the synthetic plume tomography is similar in scale, variability of anomaly shape, and vertical correlation variation to the actual P- and S-wave tomography of the northern East-African Rift, providing further support for the existence of upper-mantle plumelets below the region.

1 Introduction

Volcanic rifting is undoubtedly related to the thermal state of the mantle during extension and decompression melting (e.g. White and McKenzie, 1989), and the thermal state of the mantle can be estimated from seismic wave speeds derived from inverse models. The East African Rift is the largest active volcanic rift zone on the planet. However despite the clear evidence for decompression melting, there have been conflicting interpretations of the thermal state of the mantle below Afar and the Main Ethiopian Rift. The low seismic velocity inverted from surface waves is consistent with a hotter than average mantle, 1450 °C, or roughly 100 °C hotter than normal mantle (Armitage et al., 2015). However, a S-wave tomographic model of the Afar region found that at around 400 km depth, the S-wave velocity was lower than could be explained by a simple 100 °C thermal anomaly (Thompson et al., 2015). This can be explained if there is a certain degree of very deep partial melting which becomes retained within the mantle (Thompson et al., 2015).

Interpretations of inverse seismic models, such as the presence of very deep melt, or a vertically rising thermal plume, are rarely tested. The seismic velocity structure below the East African Rift (EAR) derived from tomographic models is complex (Civiero et al., 2015, 2016). In fact, the EAR is not unique in terms of complexity: Several recent tomographic studies have found evidence of plume complexity, including possible branching (Rickers et al., 2016), and triggering of secondary upper-mantle plumes above a lower-mantle source (Civiero et al., 2018; Goes et al., 1999; Saki et al., 2015). The apparent complexity from tomographic inversions has been interpreted to represent secondary instabilities, such as small plumes, or plumelets, rising from a stalled larger thermal anomaly

is appealing given that secondary plumes have been shown to occur within laboratory experiments (Kumagai et al., 2007, e.g.), however the hypothesis that follows from the interpretation of seismic tomographic models needs to be tested. In this study we will explore if small-scale plumes, or *plumelets*, are consistent with seismic observations. We develop a workflow to model physically plausible plumelet scenarios based on regional mantle flow. These physical structures are converted to seismic structures and are the re-resolved at the scale of the seismic experiment. This allows us to test the hypothesis that the apparent complexity in seismic tomographic images is due to complex plume-like structures within the upper mantle.

Only a few previous studies have tested the tomographic results against dynamic models to understand the nature and origin of mantle plumes, with very few using full resolution tests. Boschi et al. (2007) and Styles et al. (2011b) did a comparison of global and regional plume models against global tomography to get an overview of how many plumes might exist. Davaille et al. (2005) looked over a large region encompassing all of African and surrounding hotspots below the Atlantic and Indian Ocean, and qualitatively compared plume styles predicted from analogue models. Structures from dynamic plume models have been used by Hwang et al. (2011) and Maguire et al. (2016) to illustrate how wavefront healing may mask the travel-time signatures of plumes below 1000 km depth. Ballmer et al. (2013) performed a regional study focusing on Hawaii and found that numerical models of a complex thermo-chemical plume are compatible with the tomographic images of the upper mantle below the islands.

In this paper, we numerically generate upper-mantle upwellings from both a steady-state thermal boundary layer and from a local hot layer below 660 km depth using Earth-like parameters. We will first analyse plume scales and strength in the numerical models as a function of Rayleigh number and temperature contrast across the hot thermal boundary layer. Next, we convert the thermal models to seismic velocity using thermo-dynamic methods that account for the effects of temperature, pressure, phase, composition and anelasticity (Cobden et al., 2008; Goes et al., 2004; Styles et al., 2011a). We then use these seismic structures as input for synthetic resolution tests using the same data distribution and inversion scheme and parameters as in Civiero et al. (2015, 2016). Finally, we compare the simulated convective instabilities with our seismic observations to find (a) the parameters of the models needed to justify the spacing, scale and amplitude the seismic anomalies imaged below the rift system; (b) the type and location of the thermal boundary layer able to generate such instabilities in the upper mantle; (c) the most plausible geometry and thus the stage in temporal evolution of the two mantle plumes below Afar and MER.

1.1 Tomography on the northern East-African Rift

The P- and S-wave tomography performed by Civiero et al. (2015, 2016) imaged the mantle structure below the northern EAR using seismic stations deployed along the rift from Saudi Arabia in the north to Madagascar in the south (Fig. 1). The study region comprises Afar and the Main Ethiopian rift (MER), i.e., the northern end of EAR. This area is characterised by a topographic swell (the Ethiopian Plateau), 30 Myr old flood basalts, and currently active volcanism and extensional faulting (Fig. 1a). Seismic stations that were used are from 26 different temporary and permanent arrays that span the region from Saudi Arabia to Madagascar. This wide aperture allows for high resolution from 50 km below the study area in the box in Fig. 1a, from \sim 50 km down to between 700 and 800 km depth.

Civiero et al. (2015, 2016) performed teleseismic travel-time tomography using the method of VanDecar et al. (1995), on a data set of 16420 relative P travel times and 16569 relative S and SKS travel times. The preferred tomographic results include moderate damping to a regional surface-wave model (Fishwick, 2010) down to 300 km depth, where the limited number of crossing teleseismic rays does not provide good vertical resolution. These models, NEAR-P15 (for P-waves) and NEAR-S16 (for S- and SKS-waves), were obtained with regularisation parameters that provide a balance between misfit reduction and not overfitting the data beyond the data error estimates (using flattening=4800, smoothing= 153,600).

As illustrated in Fig. 1b and c, the tomographic inversion recovered two clusters of low-velocity anomalies, below Afar and MER, that extend from about 200 km depth to the topmost lower mantle. The P-wave model clearly illustrates that the two clusters are separate features, and required to extend through the transition zone. The sub-lithospheric low-velocities have been attributed to the spreading of plume material below the lithosphere, with local contributions from melt (Civiero et al., 2015, 2016). The deeper structures (300–660 km depth) were interpreted as plume tails. Below 700 km depth, the structure changes, in particular in the P-wave model where resolution extends somewhat deeper than in the S-wave model.

1.2 Constraints on plume spacing

Various studies have suggested that hotspot or volcanic clusters may share the same root zone. Kumagai et al. (2007) proposed that the French Polynesian hotspots (Tahiti-Macdonald-Pitcairn), the Canaries-Cape Verde-Azores-Great Meteor hotspots and the Marion-Crozet hotspots share a source comprising ponded material below 660 km depth seismic discontinuity. Saki et al. (2015), based on the analysis of transition-zone discontinuity topography from PP and SS precursors, also proposed that the Canaries-Cape Verde and Azores share a source layer below the transi-

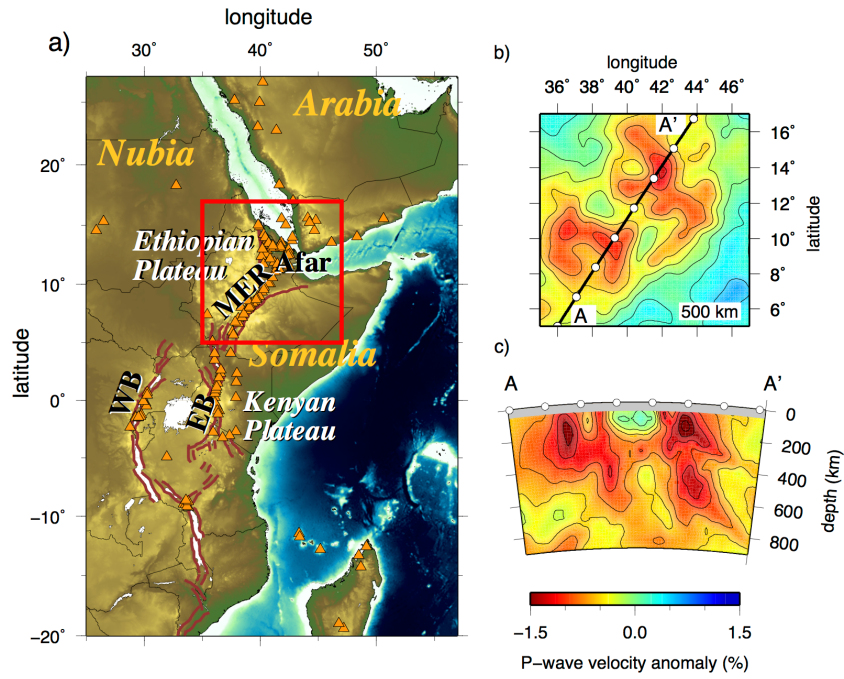


Fig. 1: Study area and tomography: (a) East African rift tomographic model, Holocene volcanoes, and active fault zones. Stations used were distributed all across the area shown (see supplement for station locations), but good resolution was obtained in the study area in the black box. (b) horizontal depth slice through the undamped P model, NEAR-P15 at 500 km depth. The black line indicates the orientation of the cross-section in c. (c) vertical cross-section through the undamped P model NEAR-P15. The cross-section illustrates two clusters of low velocity anomalies below Afar and west of the MER extending to the base of the transition zone.

tion zone. Tomographic images by Rickers et al. (2016) indicate that Iceland and Jan Mayen are two branches of a common plume below 1300 km. In all these cases, the spacing between hotspots is around 1000-150 km. Chang and Van der Lee (2011) imaged possible plume conduits below Afar, Kenya and northern Saudi Arabia that are separate down to at least 1500 km depth. Again spacing between these proposed plumes is about 1500 km.

Other examples suggest a plume spacing of hundreds of kilometers: These include our inferred Afar and MER plumelets which are separated by 400-600 km (Civiero et al., 2015, 2016), proposed *baby plumes* below the European hotspots (Eifel, Massif Central, Bohemian Massif, upper Rhine Graben, Brest Graben; Goes et al., 1999; Granet et al., 1995, which are spaced 250-400 km. Furthermore, spacing between active volcanoes within the Canaries, Cape Verde, Society Islands is between 50 and 300 km.

1.3 Dynamic controls on plume spacing

The spacing of thermal plumes that form naturally in laboratory experiments of Rayleigh Bénard convection, where the strongly temperature dependent viscous fluid is heated from the base and cooled from the top is a function of the aspect ratio of the rectangular tank and the local Rayleigh number (Androvandi et al., 2011). For fluids that have a viscosity that is an exponential function of temperature, the wavelength, or plume spacing, is observed to decrease with Ra as $\lambda/H \propto Ra^{1/3}$, where H is the height of the experimen-

tal tank (Androvandi et al., 2011). In numerical experiments where the fluid is assumed to be isoviscous, the reduction in wavelength takes the form $\lambda/H \propto Ra^{1/6}$ (Zhong, 2005; Galsa and Lenki, 2007). If we assume that the plumes initiate at ~ 1000 km depth, then the spacing of the plumes would be of the order of 1000 km or less, for a local $Ra > 10^5$ (Androvandi et al., 2011). Therefore, it follows that if the stagnation of large whole mantle plumes at shallow depth leads to the formation of secondary plumes (plumelets) due to the increased temperature at the boundary (e.g. Kumagai et al., 2007), then the spacing will be a function of the depth at which the stagnation occurs.

For the destabilisation of a layer of hot material, or the development of Rayleigh Taylor instabilities, the growth of the instability should be largest for the characteristic wavelength defined by the aspect ratio of the domain. From linear scaling analysis of the destabilisation of a layer equal to one tenth of the height of the region, H , the characteristic wavelength is $\lambda = 0.37H$ (Schmeling, 1987). This calculation is for two materials of the same viscosity. It was subsequently demonstrated that in 2D systems the final dominant wavelength is not necessarily equal to the characteristic wavelength if there was an initial perturbation to the system (Schmeling, 1987). That aside, if we assume a thin layer 100 km thick of hot mantle material ponds at the 660 km depth seismic discontinuity, then the characteristic wavelength of the plumelets would be on the order of 200 km. Given the impact of the initial configuration on the estimate of plume wavelength, we will numerically model both Rayleigh Bénard and Rayleigh

Taylor instabilities for Newtonian and non-Newtonian rheologies.

2 Dynamic models methods

2.1 Numerical models set-up

We solve Stokes equations using the numerical model Stag3D (Tackley, 1998) for the flow of a highly viscous fluid within a Cartesian domain of aspect ratios 3x3x1, 4x4x1, and 6x6x1, and the model is 700 km deep. Mechanical boundary conditions are free slip on all sides and of fixed temperature at the top and bottom. Temperature boundaries on the sides are of zero gradient. Tracers are used to make material at the top - between 0 and 0.14H depth - buoyant, by assigning them a buoyancy number, B , which equals the thermal over chemical density anomaly: $B = \Delta\rho_c/\Delta\rho_T = 0.5$ (Fouré, 2009). This depth range will comprise most of the upper thermal boundary layer that forms as the model evolves. This minimizes lithospheric participation in the convection pattern and allows us to focus on plume scales and geometry.

Temperature in the asthenosphere is initially set to 1350 °C, the assumed background mantle potential temperature. At between 0 and 100 km depth, temperature increases linearly from 0 °C to 1350 °C. At the bottom of the model we explore two setups:

- A hot lower boundary condition of 1350°C + ΔT_e , where ΔT_e is the excess temperature.
- A basal hot layer, 100 km thick, of temperature ΔT_e is included in the initial condition, and the lower boundary temperature is held at 1350 °C.

The former lower boundary condition will lead to Rayleigh Bénard convection, while the latter initial condition will destabilise in the form of Rayleigh Taylor instabilities.

The form of the convective instabilities will be determined by the rheology of the upper mantle. We test two different dominant mechanisms for mantle creep, diffusion and dislocation creep, which can be expressed as a Newtonian and a non-Newtonian rheology. The first rheology we take is an idealised temperature dependent Newtonian material written as,

$$\eta = \eta_0 A_{ref} \exp\left(\frac{E}{RT}\right) \quad (1)$$

where η_0 is the scaling viscosity, $A_{ref} = 2.2 \times 10^{-5}$ is the pre-factor, $E = 120 \text{ kJ mol}^{-1}$ is the activation energy, $R = 8.31$ is the ideal gas constant and T is mantle potential temperature. The activation energy, which was determined empirically for the upper mantle to achieve agreement between calculations and observations of lithosphere plate flexure, is a factor of 3 lower than experimentally derived estimates (Korenaga and Karato, 2008; Watts and Zhong, 2000). However, as shown by Christensen (1984) and Jaupart and

Mareschal (2011), a small value for the activation energy may be regarded as a convenient way to approximate nonlinear diffusion creep with a Newtonian analogue.

The second rheology we consider is a strain weakening non-Newtonian temperature and pressure-dependent creep law,

$$\eta = \eta_0 A_{ref}^{\frac{1}{n}} \exp\left(\frac{E + pV}{nRT}\right) I_2^{\frac{1-n}{n}} \quad (2)$$

where the pre-factor $A_{ref} = 1.47 \times 10^{-16}$ for a reference strain rate of 10^{-15} s^{-1} , $E = 523 \text{ kJ mol}^{-1}$, activation volume $V = 4 \text{ cm}^3 \text{ mol}^{-1}$, stress exponent $n = 3.6$ (Korenaga and Karato, 2008), and I_2 is the second invariant of the deviatoric strain rate tensor. Finally in both models the scaling viscosity, η_0 , is set by the initial Rayleigh number,

$$Ra = \frac{\alpha g \rho_m \Delta T H^3}{\kappa \eta_0} \quad (3)$$

where H is the height of the model domain and ΔT is the temperature difference across the model domain from top to the bottom. The remaining constants are listed in Table 1. We explore initial Ra of 10^6 to 10^8 . The various models are listed in Table 2.

3 Dynamic models plume scales and styles

For the Rayleigh Bénard experiments the model generates regularly spaced plumes for both the Newtonian and non-Newtonian rheologies (Fig. 2). These plumes grow uniformly across the model domain and the spacing is a function of the initial Ra (Fig. 3). For the temperature dependent Newtonian rheology (models N1 to N4; Table 2), rather classic mushroom shaped plumes are generated (Fig. 2a). These plumes eventually impinge on the buoyant lithosphere. The non-Newtonian model plumes are significantly thinner, with plume heads that rapidly flatten out under the lithosphere (Fig. 2b). Using the definition of Labrosse (2002) for finding the plume wavelength, we search for the distance between temperature anomalies of ,

$$T > \bar{T} + f(T_{max} - T_{min}) \quad (4)$$

where \bar{T} is the mean temperature, T_{max} is maximum temperature, T_{min} is the minimum temperature, and $f = 0.2$. As in previous studies, we find that the wavelength of the plumes is a function of the Ra number (Zhong, 2005; Galsa and Lenki, 2007; Androvandi et al., 2011). The trend in reduction in wavelength follows $\lambda/H \propto Ra^{1/6}$, however given the range in measured wavelengths we cannot rule out the possibility that $\lambda/H \propto Ra^{1/3}$, as found for laboratory experiments using fluids with a strongly temperature dependent viscosity (Androvandi et al., 2011; Fig. 3a). The two data points for the non-Newtonian rheology (models N5 and N6) would suggest a stronger dependence

Tab. 1: Model parameters

Parameter	Value	Description
B	0.5	Bouyancy number for the lithosphere
g	9.8 m s^{-2}	Acceleration due to gravity
H	700 km	Model depth
p		Pressure
Ra		Initial Rayleigh number
T		Temperature
ΔT	1350°C	Asthenosphere temperature
ΔT_e		Temperature anomaly
α	$3.3 \times 10^{-5} \text{ K}^{-1}$	Coefficient of thermal expansion
κ	$10^{-6} \text{ m}^2 \text{ s}^{-1}$	Thermal diffusivity
ρ_m	3340 kg m^{-3}	Mantle density
η_0		Scaling viscosity
Newtonian Rheology		
E	120 kJ mol^{-1}	Activation energy
A_{ref}	2.2×10^{-5}	Normalizing factor
Non-Newtonian Rheology		
E	523 kJ mol^{-1}	Activation energy
V	$4 \text{ cm}^3 \text{ mol}^{-1}$	Activation volume
n	3.6	Stress exponent
A_{ref}	1.47×10^{-16}	Normalizing factor

Tab. 2: List of models

Name	Type	Ra	ΔT_e ($^\circ\text{C}$)	Newtonian	Non-Newtonian	Aspect ratio (resolution)
N1	Rayleigh	6×10^5	100	x		6x6x1 (384x384x64)
	Bénard					
N2	Rayleigh	2×10^6	100	x		6x6x1 (384x384x64)
	Bénard					
N3	Rayleigh	6×10^6	100	x		6x6x1 (384x384x64)
	Bénard					
N4	Rayleigh	6×10^7	100	x		6x6x1 (384x384x64)
	Bénard					
N5	Rayleigh	6×10^5	100		x	6x6x1 (384x384x64)
	Bénard					
N6	Rayleigh	6×10^6	100		x	6x6x1 (384x384x64)
	Bénard					
N7	Rayleigh	6×10^6	100		x	3x3x1 (192x192x64)
	Taylor					
N8	Rayleigh	6×10^6	100		x	4x4x1 (512x512x128)
	Taylor					
N9	Rayleigh	6×10^6	200		x	4x4x1 (512x512x128)
	Taylor					
N10	Rayleigh	6×10^6	400		x	4x4x1 (512x512x128)
	Taylor					

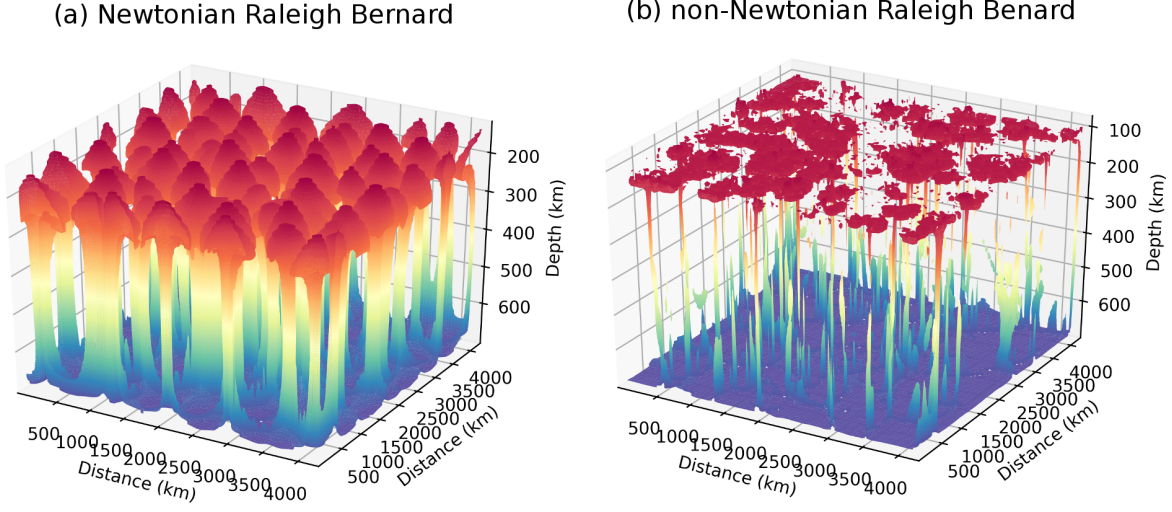


Fig. 2: Surface plots of the 1% thermal anomaly (corresponding to a temperature of 1363.5°C) coloured by depth. In both models the $\text{Ra} = 6 \times 10^6$, models N3 and N6 in Table 2. (a) Raleigh Bénard convection for a Newtonian rheology showing equally spaced plumes that developed uniformly in time. (b) Raleigh Bénard convection for a non-Newtonian rheology. In this case the strain rate dependence creates thin plumes with flat heads that rapidly impinge on the lithosphere.

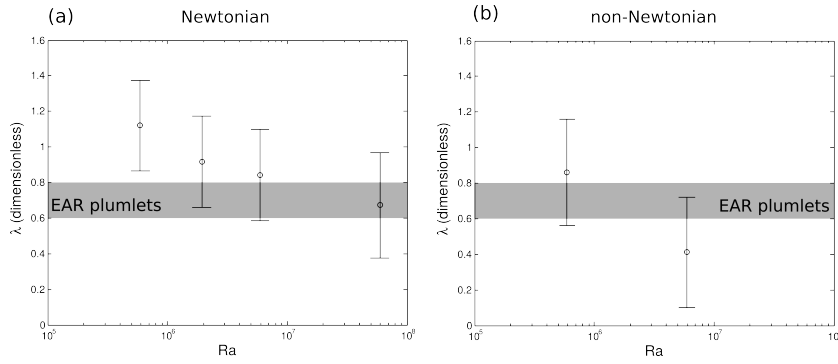


Fig. 3: Dimensionless wavelength for Rayleigh Bénard convection as a function of Raleigh number. (a) Newtonian models, showing the classic power law dependence between wavelength and Ra . The grey shaded area shows the estimate for the wavelength of the slow Vs anomalies below EAR, made dimensionless by dividing by the depth to the 660 km depth seismic discontinuity. If these instabilities are due to Raleigh Bénard convection, we would require a low viscosity (high Ra). (b) Non-Newtonian models, showing a stronger dependence on Ra . However in this case at $\text{Ra} > 10^7$, the plumes become difficult to detect given the plume tails are very thin. If the upper mantle is dominantly non-Newtonian, EAR plumlets are consistent with a higher viscosity (lower Ra).

of wavelength on Ra when compared to the Newtonian models (Fig. 3b). Unfortunately, plumes at higher $Ra > 6 \times 10^6$ were too thin to be detected.

If we scale the dimensionless wavelength by the depth to the 660 km depth seismic discontinuity we find that the possible EAR plumelets could be explained by Newtonian plumes with an upper mantle of $Ra > 10^6$ (Fig. 3a). This corresponds to a scaling viscosity, $\eta_0 < 5 \times 10^{20}$ Pas. For non-Newtonian plumes the wavelength of EAR plumelets corresponds to a Ra for the upper mantle of $\sim 10^6$, or a reference viscosity of $\eta_0 < 5 \times 10^{20}$ Pas. However, these plumes are very likely too thin to be seismically visible.

The Rayleigh Bénard convection develops uniformly. The Rayleigh Taylor destabilisation of a hot layer of material is however not uniform in time (models N7 to N10; see Fig. 4). Here we can see early and late stage plume-like structures within the same snap-shot. The spacing of these instabilities is of the order $\lambda = 0.5H$ to $\lambda = H$ depending on the aspect ratio of the model domain and the stage at which the plume forms (Fig. 4; see models N7 and N8). The first instability always forms at a corner of the model, and this subsequently leads to a destabilization of the hot layer that propagates outwards from the corner. The wavelength of the plume-like structures was found to be independent of the temperature of the hot layer, as this did not significantly affect the initial Ra number. Furthermore, the contrast in temperature is high for these plumes when compared to the Newtonian Rayleigh Bénard convection (Fig. 5). The strong temperature contrast is likely important. When the temperature gradient is low the plume becomes less visible to seismic experiments (Styles et al., 2011b). Therefore given the spacing of the Rayleigh Taylor is similar to the Rayleigh Bénard convection for the aspect ratio chosen, but the plumes have a stronger temperature contrast we will explore how they are transformed when viewed as seismic anomalies.

4 Synthetic tomography methods

4.1 Conversion to seismic anomalies

To convert the thermal plume structures into velocities and density we follow the approach of Cobden et al. (2008) and Styles et al. (2011b). We use the thermodynamic code PerPlex (Connolly, 2005) with the NCF-MAS data base stx08 (Xu et al., 2008) to calculate the elastic parameters (bulk modulus K and shear modulus G) and density as a function of pressure, temperature and composition. For the basic conversions, we assume a pyrolite composition, except for the continental lithosphere which is taken to be harzburgitic (both compositions from Xu et al., 2008). A constant adiabatic temperature gradient of 0.45 K km^{-1} (a reasonable upper mantle average, according to Styles et al., 2011b) is added to the potential temperatures from the Boussinesq model. The velocities have further been corrected for the effects of temperature-, pressure-, and hydration dependent anelasticity using composite model Q_g

(Goes et al., 2012; van Wijk et al., 2008) for a frequency of 1 Hz (which is good for the P-waves, but on the high side for the S-waves). The mantle is assumed to be damp (1000 H/Si) and the continental lithosphere dry (50 H/Si). The uncertainties involved in the calculation of elastic and anelastic parameters lead to uncertainties in V_P and V_S anomalies of around $\pm 0.1\%$ and $\pm 0.15\%$, respectively (Cammarano et al., 2003; Styles et al., 2011b).

Velocity anomalies are computed relative to a reference profile in a corner of the model (at $x = 0$, $y = 0$; e.g. Fig. 4), an area with no upwelling or downwelling. The numerical models do not include the effect of melting. To include the basic effect of melt retention, we make a simple estimate of melt fractions and their signature: The dry solidus is approximated with a linear increase from 1100°C at 0 km to 1700°C at 200 km depth (based on the variation in the solidus from Herzberg et al., 2000). Then we estimate a melt fraction from how much the actual (full) temperature exceeds the solidus, again using a linear relation where melt fraction is 0% at the solidus temperature and reaches a maximum of 2% for 300 K excess temperature. We limit the range of melt fractions, assuming that melts are mobile and much larger melt fractions will escape rather than pool (e.g. Faul et al., 1994). To get the seismic anomalies due to melting, melt fractions are multiplied with the melt derivatives from Hammond and Humphreys (2000), which are -3.6 per percent melt volume for V_P and -7.9 for V_S . This results in substantial local reductions in seismic wave speeds in the locations in the thermal structures where melt is expected.

4.2 Tomographic method

We test how the synthetic structure is imaged using the tomographic relative travel-time inversion for P- and S-wave velocity following the method of VanDecar et al. (1995). This technique cannot retrieve absolute velocities, but only anomalies relative to the average regional background. We perform a linear inversion and use ray theory which leaves some uncertainties in the determinations of the magnitude of the velocity anomaly, but should not change the overall anomaly patterns with depth (Montelli et al., 2004b). We invert for these synthetic velocity structures using the same model parameterisation, regularisation scheme and parameters and raypaths (calculated through the iasp91 1D velocity model) as used in the tomography models of Civiero et al. (2016, 2015).

The synthetic datasets comprise 16420 relative P-wave arrival times and 16569 S-wave arrival times at 452 and 379 stations, respectively, for P- and S-wave travel times. We calculate the arrival times by applying full 3D ray tracing (Julian and Gubbins, 1977) through the synthetic models and add Gaussian random noise to the synthetic data, respectively 0.07 s and 0.37 s for P- and S-wave data, i.e., of similar magnitude as the estimated errors in the real data.

The resolution in the shallower part of the upper

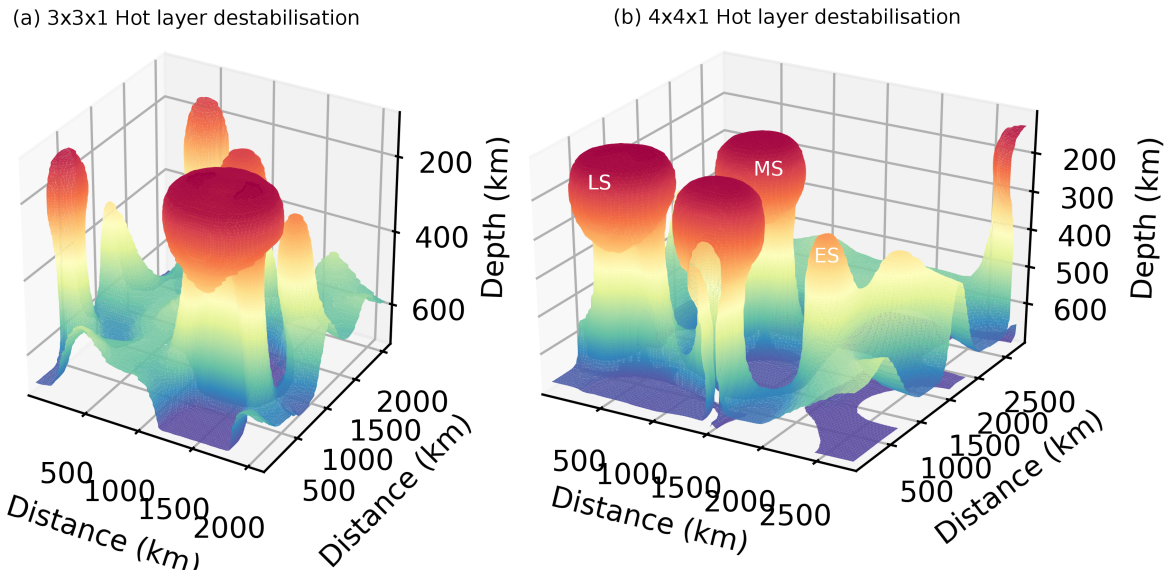


Fig. 4: Comparison of patterns of destabilisation of a $100\text{ }^{\circ}\text{C}$ hot layer for a $3\times 3\times 1$ and $4\times 4\times 1$ Cartesian box (models N7 and N8 in Table 2). Labeled are ES - earlt stage plumelet; MS - mid-stage plumelet; and L - late stage plumelet.

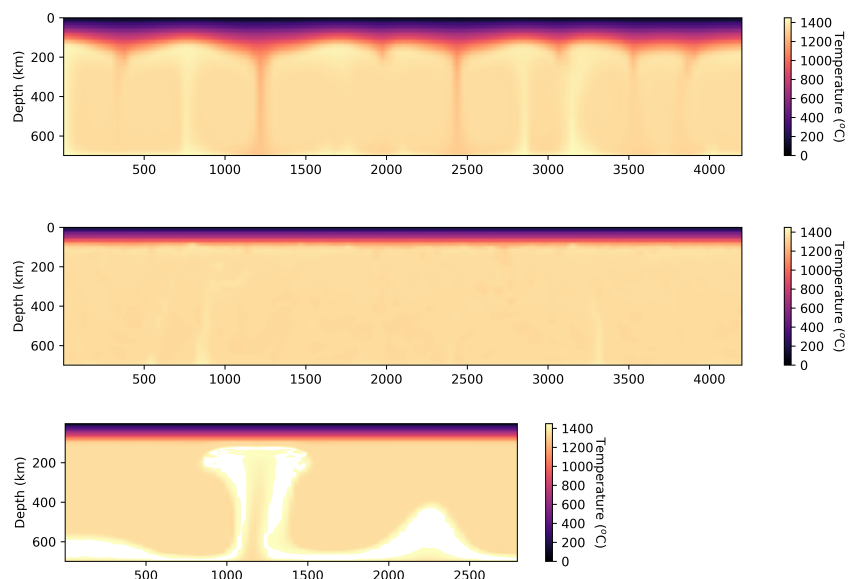


Fig. 5: Cross section of Newtonian and non-Newtonian Rayleigh Bénard models N3 and N6 and the Rayleigh Taylor model N8.

mantle (0-200 km depth) is low due to a lack of crossing rays at this depth range. In the inversion of seismic observations the 3D structure obtained from the surface-wave model of Fishwick (2010) as an additional constraint on the shallow mantle structure (Civiero et al., 2016, 2015). The P-wave speed starting model has been obtained converting the absolute shear velocities from the shear wave speeds to temperature and VP following Goes and van der Lee (2002) and assuming that the S-wave anomalies were purely thermal in nature (see Civiero et al., 2015 for further details). To mimic this in the synthetic tomography, we moderately damp the model (damping = 35) towards the synthetic structure down to 350 km. This is an optimistic test, as surface waves tomography will not retrieve the exact seismic structure; therefore, the damped version for the observed tomography is somewhere between the undamped and damped synthetic cases.

To perform the resolution tests, the numerical models need to be projected onto the tomographic grid. Because the tomographic grid is coarser than the numerical one, some of the finer scale features are not captured when the numerical model is re-sampled onto the tomographic grid. The volume of the whole tomographic model spans the range 28° N - 25.40°S in latitude, 25°E - 57.20°E in longitude and 0-2000 km in depth (shown by the black box in Fig. 6), with a node spacing respectively of 0.5°, 0.4° and 50 km. We focus our interpretation within the region (517°N and 3547°E) comprising the Afar and MER regions (blue box in Fig. 6, area outlined in Fig. 1), where we have the highest density of crossing rays. The numerical model is a box of 19° × 19° that extends from the surface up to ~800 km depth (red box in Fig. 6). Depending on the features we analyse, we rotate the model to position the different synthetic plume anomalies in the approximate locations of the two main low-velocity anomalies found in the observed P- and S-wave tomography, below Afar and west of the MER.

5 Synthetic tomography results

We focus on the Rayleigh Taylor instabilities given they have a strong temperature contrast (Fig. 5), and have a wavelength that is similar to that interpreted from the tomographic observations. We will also focus on the models with an aspect ratio of 4x4x1, as the increased numerical resolution of these models (512x512x128) allowed us to model very large temperatures contrasts between the asthenosphere and the plumelet temperatures, 100 to 400 C (models N8 to N10; Table 2)

5.1 Plume resolution

We use the model N8 (see Table 2) to illustrate the resolution of the synthetic plume structures below Afar and MER and compare the resolved models with the observed P- and S-wave tomography. We rotated the plume model in order to place a middle-stage plume with a broad head and a thick stem below Afar, a late-stage plume with a head spread at the base of the

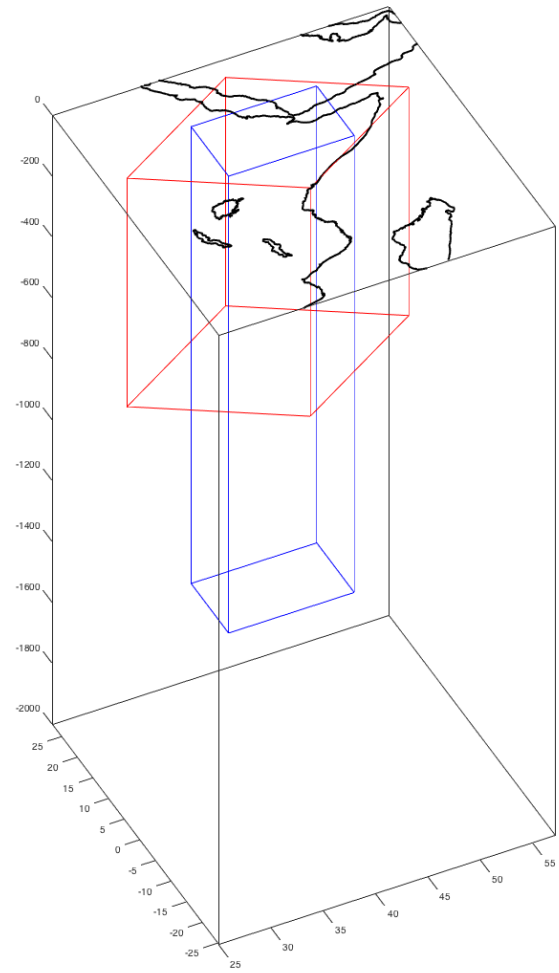


Fig. 6: 3D perspective figure illustrating the relative sizes and locations of the tomographic and numerical model boxes. The black volume is the whole volume for the tomographic inversion. The red box is the volume of the numerical model used to perform the plume resolution tests, in this case rotated by 225° with respect to the north direction. This orientation in space places the synthetic low-velocity structures at the same position as the imaged tomographic low-velocity anomalies beneath Afar and MER. The blue volume represents our region of interpretation, parameterised with a finer grid than outside.

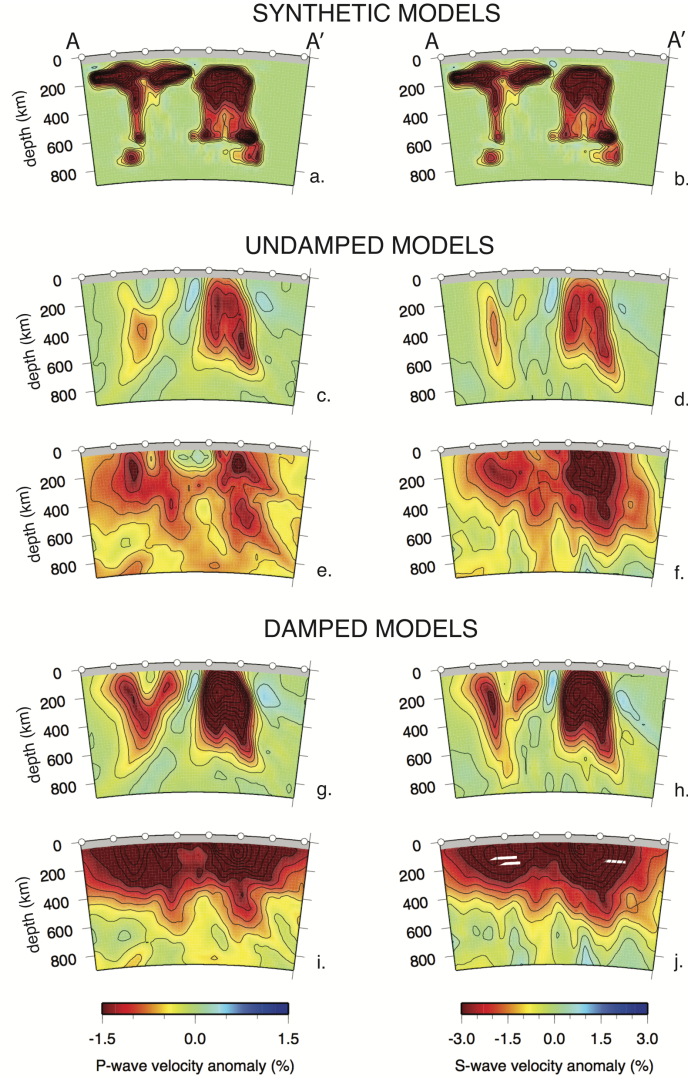


Fig. 7: (a) P-wave velocity anomalies (%) along a vertical cross-section through the input model N8 oriented such that the two plumes shown are positioned approximately under Afar and west of the MER. (b) Input S-wave velocity anomaly (%). The location of the cross-sections (black line) is shown in Fig. 1b. The structure on the right represents the synthetic middle-stage (MS) plume, the structure on the left the late-stage (LS) plume discussed in the text. (c, d, g, h) Vertical cross-sections through the recovered undamped (damping = 0) (c-d) P- (c) and S-wave (d) models and the moderately damped (damping = 35) P- (g) and S-wave (h) models. e, i) Vertical cross-sections of the undamped (e) and damped (i) NEAR-P15 model. (f, j) Vertical cross-sections of the undamped (f) and damped (j) NEAR-S16 model. The spacing between the contours is 0.25 % for P-wave models and 0.50 % for S-wave models. White points indicate distance every 2° . Both the undamped models (cd) and the damped recovered models (gf) image most of the middle-stage plume, and only the head, but with relatively subdued amplitudes, of the late stage plume. The scale of the recovered structures is quite similar to that of imaged features.

lithosphere, and a narrow tail below MER (Fig. 7a and b). Synthetic cross sections of the same orientation as the sections through models NEAR-P15 and NEAR-S16 in Fig. 1 are shown in Fig. 7c, d, g, and h. The middle-stage plume located beneath Afar are generally well recovered, although details, such as a partially folded head and a tail influenced by phase-boundary topography are not identifiable. The anomalies from the late-stage upwelling below the MER are recovered less clearly, especially in the undamped case, where the plume head, which has spread along the base of the lithosphere, is not fully resolved (Fig. 7c, d). The recovery of the plume geometries can be enhanced if constraints on the shallow structure and damping towards it are added (Fig. 7g, h; see Civiero et al., 2016, 2015). Resolution for the P- and S-wave models is visually very similar. Some of the differences between the recovery of the two plumes may be due to different resolution below Afar and MER as the data coverage is slightly higher in the first region than in the latter.

Although a Cartesian model of the destabilisation of a 100 °C hot layer (model N8) cannot be expected to match the actual imaged structures in detail, the similarities between them are striking. The scale and spacing of the modelled plumes, after accounting for the seismic resolution, is similar to the observed features. Only the low velocities at shallow depths are not as widespread in the synthetic tomography compared to the observed tomography (see Fig. 7g, h, i, j).

Interestingly, NEAR-P15 and NEAR-S16 have some differences in relative P-wave over S-wave anomaly amplitude and structure of the low-velocity anomalies below Afar and the MER (Fig. 7e, f, i, j; Civiero et al., 2016). However, similar differences occur in the synthetic tests as well: The retrieved plume structure below Afar looks more pronounced in the S- than in the P-wave model, while the structure below MER looks more discontinuous in P-wave model than in the S-wave model (Fig. 7c, d, g, h). Although resolution is similarly good for the P- and S-wave models, small differences in spatial resolution due to the added lateral resolution supplied to the S-wave velocity inversion by the SKS-wave travel times leads to differences in the relative amplitudes of the imaged structures. This might mean that observed V_P/V_S ratios represent differences in model resolution as well as possible effects due to for example melt within the asthenosphere.

5.2 Plume temperature and geometry

To test how the different plume temperatures, and plume geometries corresponding to different stages of plume evolution, might be resolved by travel-time tomography, we identify three distinct evolutionary phases for models N8 to N10 (labelled in Fig. 3b). The first is an early-stage plume (ES) that is ascending from the thermal boundary layer and penetrating into the upper mantle without a well-defined head. The second structure is a middle-stage plume (MS) with a thinner feeder column of ~ 150 km diameter and a vo-

luminous head, ~ 500 km diameter, developing in the upper mantle and has not reached the surface yet. The third is a late-stage plume (LS), which shows the classical mushroom type structure with a head spreading at the base of the lithosphere, followed by a thinner tail.

Using the model N9 that has a 200 °C thermal anomaly as an example, we firstly positioned the ES, MS, and LS plumes in turn below the Afar and MER regions. In Figs. 8 and 9 we show respectively the (undamped) P-wave models below Afar and MER. The same tests applying the moderate damping are illustrated in Supplementary Figs. S2 and S3. The P-wave inversions of the dynamic models N8 and N10 are respectively shown in Supplementary Figs. S4, S5 (undamped) and S6, S7 (damped) for Afar and Figs. S8, S9 (undamped) and S10, S11 (damped) for MER region.

The recovered images for each plume stage are complex and therefore not straightforward to interpret without knowing the input model. All the plume stems are resolved through the whole upper mantle, however without additional constraints on shallow structure, the retrieved images of the ES and LS plumes are very alike, particularly above 300 km depth. This is due to the fact that the relative travel-time tomography does not have a good sensitivity to the shallow structure (0–200 km). Thus, the head spreading at the base of the lithosphere in the LS case is almost completely lost in the inversion. Damping towards an alternatively constrained shallow structure, i.e. a 3D synthetic model down to a depth of 350 km, helps to bring out the differences between the two structures (Figs. S2, S3, S6, S7, S10 and S11). The MS plume appears more distinct from the ES and LS plumes in both undamped and damped inversions, as the upper-mantle head of the plume is broader and can be resolved laterally (Figs. 8 and 9).

Overall, the modelled plumes in model N9 (temperature anomaly of 200 °C) correlate well with the tomography-imaged features in terms of magnitude at transition-zone depths (see the profiles in Figs. 8, 9, S2 and S3). In comparison, the velocity amplitudes for a temperature anomaly of 100 °C (model N8) are weak compared to the observed structures (Figs. S4, S6, S8, S10), and the velocity amplitudes for a temperature anomaly of 400 °C (model N10) are almost double the observed seismic velocity anomaly (Figs. S5, S7, S9, S11). The instabilities originating from the high temperatures in model N10 are likely not realistic as the structure is too hot when compared to the seismic observations. It would appear that model N8 most closely matches the spatial and temporal distribution of the seismic features below the northern EAR, yet the destabilisation of a 200 °C anomaly (model N9) best matches the velocity magnitudes.

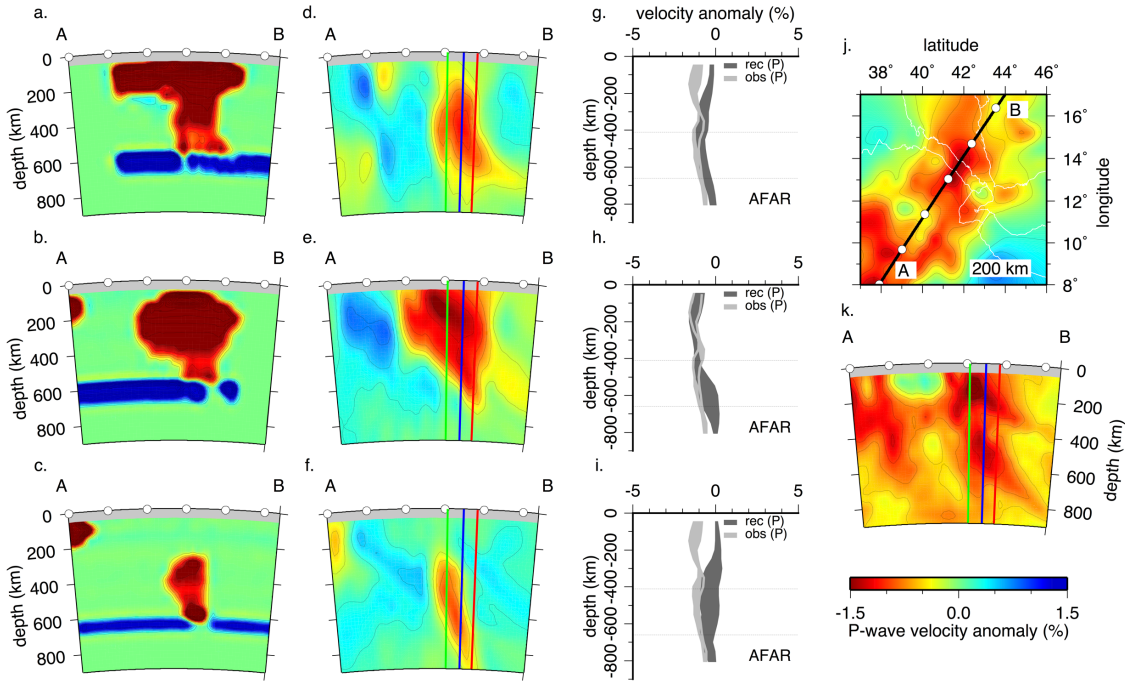


Fig. 8: Vertical cross-sections through the undamped P-wave model from case A (model N9) focused in the region below Afar. The orientation of the cross-sections (black line) is shown in the 200 km depth slices through the NEAR-P15 tomographic model j. (a, d) synthetic and resolved images of the LS phase of plume evolution; (b, e) synthetic and resolved images of the MS phase of plume evolution; (c-f) synthetic and resolved images of the ES phase of plume evolution. The imaged EP (g-j) and LP (i-l) phases are similar although the synthetic structures (a, c) are different due to the lack of resolution at shallow upper-mantle depths. The MS phase (e) is well resolved because the head of the input model (b) is relatively large. g-i) Input and retrieved P-wave velocity LS (g), MS (h) and ES (i) anomaly envelopes (%) along the green, blue and red profiles drawn in the cross-sections. Within the transition zone the retrieved and observed velocity anomalies overlap. (j) 200 km depth slice through the undamped NEAR-P15 model k) Vertical cross-section of the undamped NEAR-P15 model. The spacing between the contours is 0.25 %. White points indicate the distance every 2° .

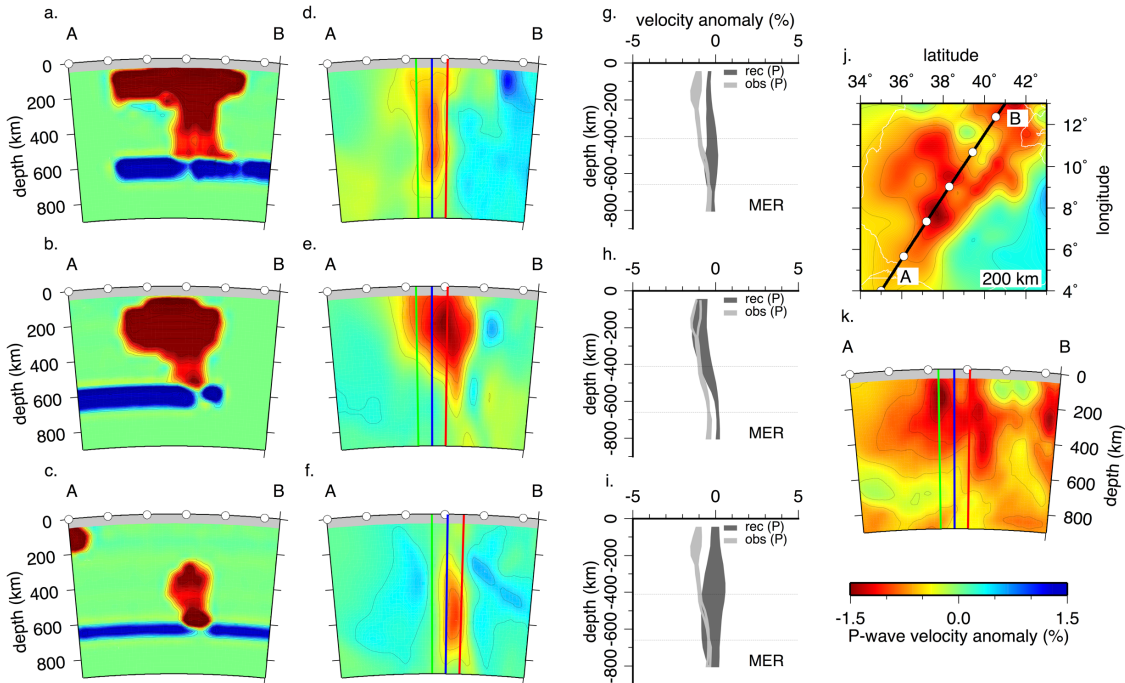


Fig. 9: Vertical cross-sections through the undamped P-wave model from case A. (d-i) focused in the region below MER. The orientation of the cross-sections (black line) is shown in the 200 km depth slices through the NEAR-P15 tomographic model j. (a, d) synthetic and resolved images of the LS phase of plume evolution; (b, e) synthetic and resolved images of the MS phase of plume evolution; (c-f) synthetic and resolved images of the ES phase of plume evolution. g-i) Input and retrieved P-wave velocity LS (g), MS (h) and ES (i) anomaly envelopes (%) along the green, blue and red profiles drawn in the cross-sections. (j) 200 km depth slice through the undamped NEAR-P15 model k) Vertical cross-section of the undamped NEAR-P15 model. The spacing between the contours is 0.25 %. White points indicate the distance every 2°.

6 Discussion

6.1 Secondary plumes or destabilisation of ponded plume material

We infer that a significant temperature excess from a thermal boundary layer is needed to match the amplitude of the upper-mantle low-velocity anomalies imaged in our observed tomography. Yet, it is difficult to reconcile the seismic signatures with a steady-state thermal boundary layer. The Rayleigh Bénard instabilities are either too diffuse (Newtonian models N1 to N4; Fig. 3a) or create anomalies that are too thin (non-Newtonian models N5 and N6; Fig. 3b), such that the thermal anomalies are seismically invisible or relatively weak (e.g. Goes et al., 2004). It is only for the Rayleigh Taylor models (N7 to N10) that thermal anomalies are sufficiently strong such that the seismic velocity anomaly is resolved in the synthetic tomography. This is a strong statement, as it implies that the plumelets are more than secondary thermal instabilities rising off a large whole mantle plume (e.g. Kumagai et al., 2007, 2008). Rather the plumelets are of the same material as the large scale plume, which has stagnated at depth and then become sufficiently buoyant to rise further in the form of a Rayleigh Taylor-like destabilization.

A viscosity contrast in the mantle will act as a barrier to a thermal or thermo-chemical plume. This results in the heating of the boundary between the two layers, and the generation of secondary plumes (Kumagai et al., 2007). This process is therefore similar to the Rayleigh Bénard numerical models in Fig. 2, and Fig. 5, which are either too diffuse or thin to be seismically imaged. Thermal-chemical plumes will stagnate if the compositional buoyancy is such that they become of equal density with the surrounding mantle. The chemical component of the plume will subsequently fall down back into the lower mantle (Kumagai et al., 2008). It is possible that some of the chemical heterogeneity becomes entrained within the thermal upwelling, but again these plumes are not the equivalent of the Rayleigh Taylor numerical models that more closely match the seismic observations.

What we require is the arrival of some distinct buoyant material at between 1000 and 660 km depth below East Africa, as for example imaged within the cluster analysis of five global S-wave tomographic models (Cottaar and Lekic, 2016). This material subsequently destabilizes and rises to form the plumelets observed within the tomographic images. The arrival of deep plume material below the Afar is consistent with the Helium isotope record of this region, which is suggestive of the melting of a deep mantle source (Pik et al., 1999). The volumetric quantity of this melting might signify a greater percentage of lower mantle than can be delivered by entrainment alone. Yet, the scenario of Rayleigh Taylor instabilities could occur if the large scale thermal-chemical plumes are also internally heated (Fourel et al., 2017). In this case the large scale plume rises until it becomes neutrally buoyant. As

it stagnates, internal heating will increase its temperature allowing for further destabilisation. The tomographic images of the upper mantle are most consistent with distinct, fat, thermal anomalies, which is consistent with models that include distinct density layers and internal heating (Fourel et al., 2017).

6.2 Different or similar evolutionary stage plumes below Afar and MER?

Comparing forward models with observed tomography to find a good matching between synthetic and observed features is not straightforward. Tomographic resolution is spatially variable and highly non-linear, making it difficult to assess (Rawlinson et al., 2010). However, from our set of resolution tests for each plume stage of evolution, we clearly recognize that models with a strong tail, like ES and LS plumes, do not match our observations well in character or amplitude profiles with depth (Fig. 8 and 9). LS plumes also do not fit the observed tomography as they do not produce sufficient transition-zone anomalies imaged below both Afar and MER (Fig. ??). Plumes in a middle phase of evolution (MS) with a broad head and a short tail best explain the evolutionary stage of both the upper-mantle structures below Afar and MER (Fig. 10). A MS plume below Afar matches the amplitude of both the P- and S-wave low-velocity anomalies within the transition zone and above (Fig. 10 q, r). Moreover, the similarity between the retrieved and observed tomographic shape of the plume is striking, especially for the S-waves (Fig. 10). The plume below MER could be in a slightly more advanced stage with a pronounced head spread at the base of the lithosphere and a quite thin (~ 100 km diameter) tail. Yet given the simplicity of the Cartesian input model, we would still suggest that the structure below the MER represents a middle stage plumelet.

From our undamped synthetic models, the amplitude of the anomalies match quite well within the transition zone while in the uppermost mantle the observed tomographic images show much stronger anomalies compared to the synthetic models from synthetics (Fig. 10 s, t). However, applying a moderate damping to the inversions in order to better retrieve the shallow velocity anomalies, we find a better match in amplitude between the models throughout the upper mantle (see Figure S13 s, t). In addition, in the damped case the shape of the anomaly is more consistent with the tomographic image of the MER plume, showing a largely widespread head in the topmost upper mantle, and a narrow stem within the transition zone. Overall, the resolution tests indicate that the two plumes below Afar and MER differ little in terms of geometry and similar stages of evolution are required to match the shapes and magnitudes.

The tomographic S-wave anomaly below Afar in NEAR-S16 is much stronger in velocity amplitude compared to that beneath MER. This prominent feature is not imaged in the recovered synthetic models. In addition, some localized strong low-velocity bodies appear

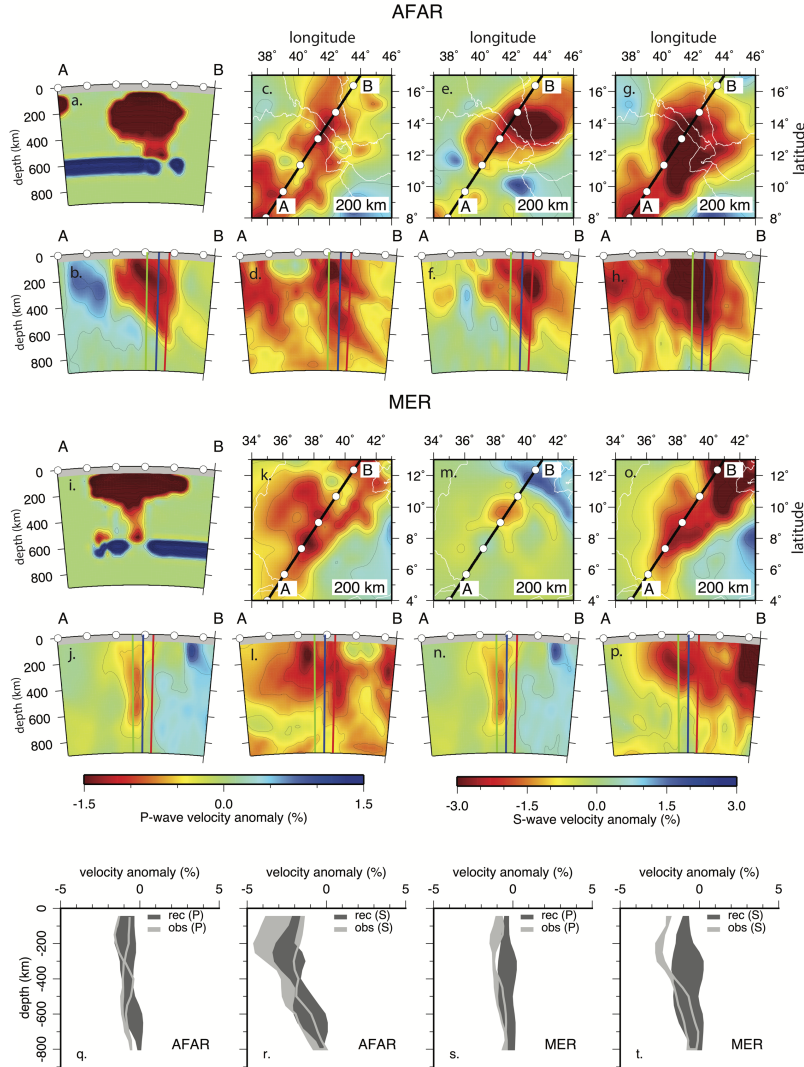


Fig. 10: Resolution tests for the dynamic plume model N9 shifted and rotated so as to position a mid-stage plume below Afar and a later-stage plume west of the MER. a, b) Cross-sections of the synthetic (a) and resolved (b) P-wave MS plume located below Afar. The cross-section of the S-wave input plume is not shown as it is similar with higher amplitude. e, f) 200 km depth slice (f) and cross-section (e) of the recovered plume. c, d) slice at 200 km depth (c) and cross-section (d) of the undamped P-wave tomographic model. g, h) slice at 200 km depth (g) and cross-section (h) of the undamped S-wave tomographic model. i, j) Cross-sections of the synthetic (a) and resolved (b) P-wave later-stage plume located below.

in the upper mantle of our tomographic model below MER. To reconcile this seismic signature the strong low V_S could be due to non-thermal heterogeneity such as melt retention in the upper mantle. As shown in the Supplementary Figure S14, we test the cases of a model with additional small-scale quantities of melt located directly below Afar and MER at different depth levels in the upper mantle at 75 km and 185 km depth (c.f. Thompson et al., 2015). Indeed, a signature of partial melt above the transition zone may be invoked as additional contribution to such velocity anomalies in order to match the S-wave anomalies, especially below Afar where the S-wave features are as strong as -5 %, almost double those below MER. The presence of melt at the lithospheric depths (< 50-70 km) would further enhance shallow anomalies adding to this contrast in anomaly strength.

7 Conclusions

We find that the seismic structure seen in the upper mantle below Afar is similar in character, scale, and amplitude to what dynamic models predict for mantle plumelets originating from a 200 °C excess temperature layer near the top of the lower mantle. This suggests that large scale mantle plumes rise upwards towards the upper mantle where they can stabilise. Subsequently due to the combination of chemical heterogeneity and internal heating, the structure will destabilise further into the upper mantle and express itself as plumelets with a spacing that is a function of the depth at which the structure stabilises and its width. Below East African Rift it would appear that the African Superplume stabilised at some point in the Earth's geological past at around 1000 to 660 km, and subsequently it has destabilised and is currently rising beneath at least Afar and the Main Ethiopian Rift in the form of a Raleigh Taylor instability.

The synthetic tomography generated from the 3D models of Rayleigh Taylor instabilities highlight that plumes have complex signatures in tomographic images. This suggests that checkerboard tests and simple vertical cylindrical features used as model inputs are insufficient to test interpretations of tomographic images. In particular, if several small-scale plumes are active below a region, and they are in different stages of their evolution, as predicted in our dynamic models, there will be complexities in both geometry and amplitude of the recovered synthetic tomography. This may explain the upper-mantle low-velocity anomalies that differ in shape from simple near-vertical cylindrical structures under a wide number of hotspot regions on scales of several 100 km in the central Atlantic (Azores, Canaries, Cape Verde, Madeira and Great Meteor), an irregularly shaped anomaly of low P-wave velocities in the shallowest 200 km, which slants north-east and downward to the top of the transition zone is imaged (Vinnik et al., 2012; Yang et al., 2006), beneath Central Europe where the low-speed anomalies show more than one branch in the upper mantle (Mas-

sif Central/Eifel; Granet et al., 1995; Ritter et al., 2001 and Indian Ocean (Marion/Crozet) where several tilted upper-mantle upwellings are suggested to rise from transition-zone depths (Davaille et al., 2005; Montelli et al., 2004a). Given that other regions exhibit similarly complex upper mantle structure and/or spacing between volcanic centres, it would be worthwhile re-analysing some previously published tomographic images below hotspots in this light.

Acknowledgments

CC was supported by a Janet Watson Fellowship from the Department of Earth Science and Engineering at Imperial College, JA is funded by ANR Accueil de Chercheurs de Haut Niveau grant InterRift. GMT (Wesse and Smith, 1995) software was used to plot Figs. 1, and 7 to 10.

References

- Androvandi, S., Davaille, A., Limare, A., Fouquerier, A., Marais, C., 2011. At east three scales of convection in a mantle with strongly temperature dependent viscosity. *Physics of the Earth and Planetary Interiors* 188, 132–141, doi: 10.1016/j.pepi.2011.07.004.
- Armitage, J. J., Ferguson, D. J., Goes, S., Hammond, J. O. S., Calais, E., Rychert, C. A., Harmon, N., 2015. Upper mantle temperature and the onset of extension and break-up in Afar, Africa. *Earth and Planetary Science Letters* 418, 78–90, doi: 10.1016/j.epsl.2015.02.039.
- Ballmer, M. D., Ito, G., Wolf, C. J., Solomon, S. C., 2013. Double layering of a thermochemical plume in the upper mantle beneath Hawaii. *Earth and Planetary Science Letters* 376, 155–164, doi:10.1016/j.epsl.2013.06.022.
- Boschi, L., Becker, T. W., Steinberger, B., 2007. Mantle plumes: Dynamic models and seismic images. *Geochemistry Geophysics Geosystems* 8, 1–20, doi: 10.1029/2007GC001733.
- Cammarano, F., Goes, S., Vacher, P., Giardini, D., 2003. Inferring upper-mantle temperatures from seismic velocities. *Physics of the Earth and Planetary Interiors* 138, 197–222, doi: 10.1016/S0031-9201(03)00156-0.
- Chang, S. J., Van der Lee, S., 2011. Mantle plumes and associated flow beneath Arabia and East Africa. *Earth and Planetary Science Letters* 302, 448–454, doi: 10.1016/j.epsl.2010.12.050.
- Christensen, U. R., 1984. Convection with pressure and temperature-dependent non-newtonian rheology. *Geophysical Journal of the Royal Astronomical Society* 77, 343–384.

- Civiero, C., Goes, S., Hammond, J. O. S., Fishwick, S., Ahmed, A., Ayele, A., Doubre, C., Goitom, B., Keir, D., Kendall, J. M., Leroy, S., Ogubazghi, G., Rümpker, G., Stuart, G. W., 2016. Small-scale thermal upwellings under the northern East African Rift from S travel time tomography. *Journal of Geophysical Research* 121, 7395–7408, doi: 10.1002/2016JB013070.
- Civiero, C., Hammond, J. O. S., Goes, S., Fishwick, S., Ahmed, A., Ayele, A., Doubre, C., Goitom, B., Keir, D., Kendall, J. M., Leroy, S., Ogubazghi, G., Rümpker, G., Stuart, G. W., 2015. Multiple mantle upwellings in the transition zone beneath the northern East-African Rift system from relative P-wave travel-time tomography. *Geochemistry, Geophysics, Geosystems* 16, 2949–2986, doi: 10.1002/2015GC005948.
- Civiero, C., Strak, V., Custódio, S., Silviera, G., Rawlinson, N., Arroucau, P., Corela, C., 2018. A common deep source for upper-mantle upwellings below the Ibero-western Maghreb region from teleseismic P-wave travel-time tomography. *Earth and Planetary Science Letters* 499, 157–172, doi: 10.1016/j.epsl.2018.07.024.
- Cobden, L., Goes, S., Cammarano, F., Connelly, J. A. D., 2008. Thermochemical interpretation of one-dimensional seismic reference models for the upper mantle: Evidence for bias due to heterogeneity. *Geophysical Journal International* 175, 627–648, doi: 10.1111/j.1365-246X.2008.03903.x.
- Connolly, J. A. D., 2005. Computation of phase equilibria by linear programming: A tool for geodynamic modelling and its application to subduction zone decarbonation. *Earth and Planetary Science Letters* 236, 524–541, doi:10.1016/j.epsl.2005.04.033.
- Cottaar, S., Lekic, V., 2016. Morphology of seismically slow lower-mantle structures. *Geophysical Journal International* 207, 1122–1136, doi: 10.1093/gji/ggw324.
- Davaille, A., Stutzmann, E., Silveira, G., Besse, J., Courtillot, V., 2005. Convective patterns under the indo-atlantic "box". *Earth and Planetary Science Letters* 239, 233–252, doi: 10.1016/j.epsl.2005.07.024.
- Faul, U. H., Toomey, D. R., Waff, H. S., 1994. Intergranular basaltic melt is distributed in thin, elongated inclusions. *Geophysical Research Letters* 21, 29–32.
- Fishwick, S., 2010. Surface wave tomography: imaging of the lithosphere-asthenosphere boundary beneath central and southern africa? *Lithos* 120, 63–73, doi: 10.1016/j.lithos.2010.05.011.
- Fouriel, L., 2009. Stabilité et instabilité de la lithosphère continental. Ph.D. thesis, Institut de Physique du Globe de Paris, 1 rue Jussieu, Paris, 75005, Paris.
- Fouriel, L., Limare, A., Jaupart, C., Surducan, E., Farinetani, C. G., Kamniski, E. C., Neamtu, C., Surducan, V., 2017. The earth's mantle in a microwave oven: thermal convection driven by a heterogeneous distribution of heat sources. *Experiments in Fluids* 58 (90), doi: 10.1007/s00348-017-2381-3.
- Galsa, A., Lenki, L., 2007. Quantitative investigation of physical properties of mantle plumes in three-dimensional numerical models. *Physics of Fluids* 19 (116601), doi: 10.1063/1.2794284.
- Goes, S., Armitage, J. J., Harmon, N., Huismans, R., Smith, H., 2012. Low seismic velocities below mid-ocean ridges: Attenuation vs. melt retention. *Journal of Geophysical Research* 117, B12403, doi: 10.1029/2012JB009637.
- Goes, S., Cammarano, F., Hansen, U., 2004. Synthetic seismic signature of thermal mantle plumes. *Earth and Planetary Science Letters* 218, 403–419, doi: 10.1016/S0012-821X(03)00680-0.
- Goes, S., Spakman, W., Bijwaard, H., 1999. A lower mantle source for central European volcanism. *Science* 286, 1928–1931, doi: 10.1126/science.286.5446.1928.
- Goes, S., van der Lee, S., 2002. Thermal structure of the North American uppermost mantle inferred from seismic tomography. *Journal of Geophysical Research* 107 (B3), 11159–11169, doi: 10.1029/1999JB900300.
- Granet, M., Wilson, M., Achauer, U., 1995. Imaging a mantle plume beneath the French Massif Central. *Earth and Planetary Science Letters* 136, 281–296, doi: 10.1016/0012-821X(95)00174-B.
- Hammond, W. C., Humphreys, E. D., 2000. Upper mantle seismic wave velocity: Effects of realistic partial melt geometries. *Journal of Geophysical Research* 105, 10975–10986.
- Herzberg, C., Raterron, P., Zhang, J., 2000. New experimental observations on the anhydrous solidus for peridotite KLB-1. *Geochemistry Geophysics Geosystems* 1 (1051), doi: 10.1029/2000GC000089.
- Hwang, Y. K., Ritsema, J., van Keken, P. E., Goes, S., Styles, E., 2011. Wavefront healing renders deep plumes seismically invisible. *Geophysical Journal International* 187, 273–277, doi: 10.1111/j.1365-246X.2011.05173.x.
- Jaupart, C., Mareschal, J., 2011. Heat Generation and Transport in the Earth. Cambridge University Press, Cambridge, UK.
- Julian, B. R., Gubbins, D., 1977. Three dimensional seismic ray tracing. *Journal of Geophysics* 43, 95–114.

- Korenaga, J., Karato, S. I., 2008. A new analysis of experimental data on olivine rheology. *Journal of Geophysical Research* 113 (B02403), doi:10.1029/2007JB005100.
- Kumagai, I., Davaille, A., Kurita, K., 2007. On the fate of thermally buoyant mantle plumes at density interfaces. *Earth and Planetary Science Letters* 254, 180–193, doi: 10.1016/j.epsl.2006.11.029.
- Kumagai, I., Davaille, A., Kurita, K., Stutzmann, E., 2008. Thin, fat, successful, or failing? constraints to explain hot spot volcanism through time and space. *Geophysical Research Letters* 35 (L16301), doi: 10.1029/2008GL035079.
- Labrosse, S., 2002. Hotspots, mantle plumes and core heat loss. *Earth and Planetary Science Letters* 199, 147–156, doi: 10.1016/S0012-821X(02)00537-X.
- Maguire, R., Ritsema, J., van Keken, P. E., Fichtner, A., Goes, S., 2016. P- and S-wave delays caused by thermal plumes. *Geophysical Journal International* 206, 1169–1178, doi: 10.1093/gji/ggw187.
- Montelli, R., Nolet, G., Dahlen, F., Masters, G., Engdahl, E. R., Hung, S. H., 2004a. Finite-frequency tomography reveals a variety of plumes. *Science* 303, 338–343, doi: 10.1126/science.1092485.
- Montelli, R., Nolet, G., Masters, G., Engdahl, E. R., Hung, S. H., 2004b. Global P and PP traveltimes tomography: Rays versus waves. *Geophysical Journal International* 158, 637–654, doi: 10.1111/j.1365-246X.2004.02346.x.
- Pik, R., Deniel, C., Coulon, C., Yirgu, G., Marty, B., 1999. Isotopic and trace element signatures of Ethiopian flood basalts: Evidence for plume-lithosphere interactions. *Geochimica et Cosmochimica Acta* 63, 2263–2279.
- Rawlinson, N., Pozgay, S., Fishwick, S., 2010. Seismic tomography: A window into deep Earth. *Physics of the Earth and Planetary Interiors* 178, 101–135, doi: 10.1016/j.pepi.2009.10.002.
- Rickers, F., Fichtner, A., Trampert, J., 2016. The Iceland-Jan Mayen plume system and its impact on mantle dynamics in the North Atlantic region: Evidence from full-waveform inversion. *Earth and Planetary Science Letters* 367, 39–51, doi: 10.1016/j.epsl.2013.02.022.
- Ritter, J. R. R., Jordan, M., Christensen, U. R., Achauer, U., 2001. A mantle plume below the Eifel volcanic fields, Germany. *Earth and Planetary Science Letters* 186, 7–14, doi: 10.1016/S0012-821X(01)00226-6.
- Saki, M., Thomas, C., Nippes, S. E. J., Lessing, S., 2015. Topography of upper mantle seismic discontinuities beneath the North Atlantic: the Azores, Canary and Cape Verde plumes. *Earth and Planetary Science Letters* 409, 193–202, doi: 10.1016/j.epsl.2014.10.052.
- Schmeling, H., 1987. On the relation between initial conditions and late stages of Rayleigh-Taylor instabilities. *Tectonophysics* 133, 65–80, doi: 10.1016/0040-1951(87)90281-2.
- Styles, E., Davies, D. R., Goes, S., 2011a. Mapping spherical seismic into physical structure: Biases from 3-D phase-transition and thermal boundary-layer heterogeneity. *Geophysical Journal International* 184, 1371–1378, doi: 10.1111/j.1365-246X.2010.04914.x.
- Styles, E., Goes, S., van Keken, P. E., Ritsema, J., Smith, H., 2011b. Synthetic images of dynamically predicted plumes and comparison with a global tomographic model. *Earth and Planetary Science Letters* 311, 351–363, doi: 10.1016/j.epsl.2011.09.012.
- Tackley, P. J., 1998. Self-consistent generation of tectonic plates in three-dimensional mantle convection. *Earth and Planetary Science Letters* 157, 9–22, doi: 10.1016/S0012-821X(98)00029-6.
- Thompson, D. A., Hammond, J. O. S., Kendall, J. M., Stuart, G. W., Helffrich, G., Keir, D., Ayele, A., Goitom, B., 2015. Hydrous upzelling across the mantle transition zone beneath the Afar Triple Junction. *Geochemistry Geophysics Geosystems* 16, 834–846, doi: 10.1002/2014GC005648.
- van Wijk, J., van Hunen, J., Goes, S., 2008. Small-scale convection during continental rifting: Evidence from the Rio Grande rift. *Geology* 36, 575–578, doi: 10.1130/G24691A.1.
- VanDecar, J. C., James, D. E., Assumpcao, M., 1995. Seismic evidence for a fossil mantle plume beneath South America and implications for plate driving forces. *Nature* 378, 25–31, doi: 10.1038/378025a0.
- Vinnik, L., Silveira, G., Kiselev, S., Farra, V., Weber, M., Stutzmann, E., 2012. Cape Verde hotspot from the upper crust to the top of the lower mantle. *Earth and Planetary Science Letters* 319–320, 259–268, doi: 10.1016/j.epsl.2011.12.017.
- Watts, A. B., Zhong, S., 2000. Observations of flexure and the rheology of oceanic lithosphere. *Geophysical Journal International* 142, 855–875.
- Wesse, P., Smith, H. F., 1995. New version of the generic mapping tools. *EOS* 76, 329–336, doi: 10.1029/95EO00198.
- White, R. S., McKenzie, D. P., 1989. Magmatism at rift zones: the generation of volcanic continental margins and flood basalts. *Journal of Geophysical Research* 94, 7685–7729.
- Xu, W., Lithgow-Bertelloni, C., Sixtrude, L., Ritsema, J., 2008. The effect of bulk composition and temperature on mantle seismic structure. *Earth and Planetary Science Letters* 275, 70–79, doi: 10.1016/j.epsl.2008.08.012.

Yang, T., Shen, Y., van der Lee, S., Solomon, S. C., Hung, S. H., 2006. Upper mantle structure beneath the Azores hotspot from finite-frequency seismic tomography. *Earth and Planetary Science Letters* 250, 11–26, doi: 10.1016/j.epsl.2006.07.031.

Zhong, S., 2005. Dynamics of thermal plumes in three-dimensional isoviscous thermal convection. *Geophysical Journal International* 162, 289–300, doi: 10.1111/j.1365-246X.2005.02633.x.